# Adaptive Control and Scaling Approach for the Emulation of Dynamic Sub-scale Torque Loads

Santino J. Bianco[*] and Donald L. Simon.[†]
*NASA Glenn Research Center, Cleveland, Ohio, 44135, USA*

Elyse D. Hill[‡]
*Oak Ridge Associated Universities, Oak Ridge, Tennessee, 37831, USA*

Previous research by the authors proposed a control and scaling approach for emulating dynamic sub-scale torque loads. This approach produced an emulation controller that successfully regulated the dynamic behavior of a sub-scale electro-mechanical system intended to be a dynamical representation of the sub-scale turboelectric powertrain of a single-aisle commercial aircraft. The sub-scale system provides an environment without turbomachinery or rotors for the initial testing of electrified aircraft propulsion (EAP) control algorithms as they would be applied to a full-scale EAP system. The sub-scale turbomachinery/rotor torque loads were produced by electric machines (EMs) driven by the control and scaling approach, a full-scale turboelectric powertrain model, and an advanced EAP control algorithm. Although successfully tested, this approach produces an emulation controller that does not guarantee asymptotic stability. Modifying the original control law and integrating adaptive control techniques into the emulation controller allows the designer to guarantee asymptotic stability. This paper introduces the idea behind the emulation controller modifications, derives the controller, proves asymptotic stability, describes the implementation of the controller on a sub-scale electro-mechanical system intended to represent a parallel hybrid-electric turbofan engine, and describes the testing of a full-scale advanced EAP control algorithm. The turbofan engine and emulation controller performance are compared to results obtained using the previous, non-adaptive control and scaling approach.

## I. Nomenclature

| | | |
|---|---|---|
| $\alpha$ | = | speed scalar |
| $\beta$ | = | torque scalar |
| $B$ | = | angular viscous damping coefficient, lbf-ft-s |
| $i$ | = | sample number |
| $J$ | = | angular inertia, lbf-ft-s$^2$ or slugs-ft$^2$ |
| $K_P$ | = | proportional gain |
| $K_I$ | = | integral gain |
| $K_D$ | = | derivative gain |
| $\eta$ | = | switching gain |
| $\Phi$ | = | boundary layer gain |
| $N$ | = | total number of samples |
| $\omega$ | = | angular speed, rad/s |
| RE | = | relative error, % |
| RMSRE | = | root-mean-squared relative error, % |
| $s$ | = | sliding function, lbf-ft-s |
| $T$ | = | torque, lbf-ft |
| $u_{eq}$ | = | nominal or equivalent portion of control input, lbf-ft |

---

[*]AST, Control Systems, Intelligent Control and Autonomy Branch, 21000 Brookpark Rd. Cleveland, Ohio 44135, USA, and AIAA Member.

[†]AST, Control Systems, Intelligent Control and Autonomy Branch, 21000 Brookpark Rd. Cleveland, Ohio 44135, USA.

[‡]NASA Postdoctoral Program Fellow, Intelligent Control and Autonomy Branch, 21000 Brookpark Rd. Cleveland, Ohio 44135, USA.

| $V$ | = | Lyapunov function |
|---|---|---|
| $x$ | = | general variable |
| $\gamma$ | = | learning rate |
| $\dot{}$ | = | time derivative |
| $\hat{}$ | = | estimated parameter |
| $\sim$ | = | error parameter |
| max() | = | maximum |
| sat() | = | saturation function |
| sign() | = | signum function |

Subscripts

| $ASMICS$ | = | adaptive sliding mode impedance controller with scaling |
|---|---|---|
| $E$ | = | turbomachinery model |
| $G$ | = | electric machine mechanically coupled to spool in model |
| $HIL$ | = | hardware-in-the-loop |
| $M$ | = | emulation electric machine |
| $P$ | = | rig shaft |
| $SIL$ | = | software-in-the-loop |
| $SMICS$ | = | sliding mode impedance controller with scaling |
| $s$ | = | scaled |

## II. Introduction

THE electrification of propulsion systems is a primary goal of the transportation industry into the near future [1, 2]. Initiated by automobile manufacturers, electrification aims to increase the efficiency, operability, and performance of propulsion systems while decreasing industry's reliance on fossil fuels as the primary energy source. In this paper, the scope of electrification is defined as the integration of high-power electrical systems with existing mechanical systems. The purpose is to augment the operation of the existing fossil fuel-powered propulsion system, distribute propulsive power, and optimize propulsion system operation. The interest in electrification extends to all segments of the the aviation industry [3, 4], where large research efforts between the private sector, government, and academia exist to explore the electrification of gas turbine engines or the replacement of the fossil fuel-powered propulsion systems entirely [5].

The introduction of a high-power electrical system into the propulsion system introduces a number of challenges along with the desired benefits. The introduction of an electrical system increases the complexity of the powertrain. The complexity introduced by the expanded propulsion system includes the addition of actuators, primarily in the form of electric machines (EMs), which can be leveraged through control to better manage system operability and performance. More actuators capable of affecting the propulsion system means that a control system can have a greater influence on its operation. However, increased control authority necessitates the use of advanced, sophisticated control systems to manage the propulsion system operation. As with other propulsion subsystems, the control system is developed and thoroughly tested in incremental phases starting with reduced order models and advancing toward hardware-in-the-loop tests and eventually product deployment. This process is visually described in Fig. 1. The process typically begins with modeling and simulation in a software-in-the-loop environment. Partial hardware-in-the-loop tests follow that
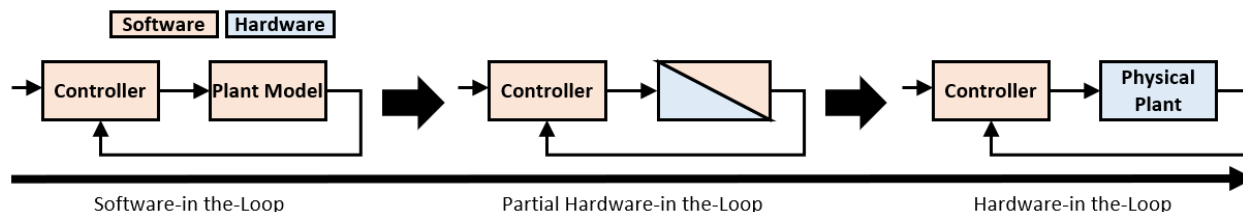


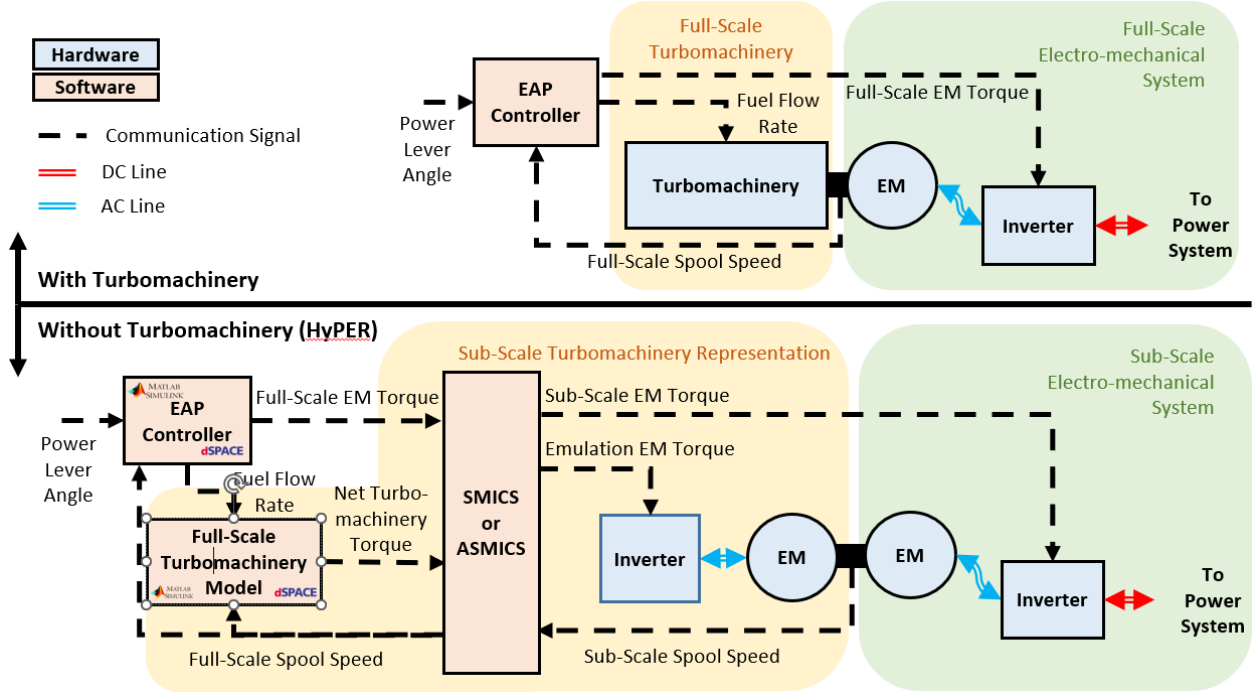**Fig. 1   General example of a control system verification process.**

2

**Fig. 2  Example of EAP controller implementation on a hybrid-electric gas turbine engine with and without turbomachinery present.**

incrementally and systematically replace previously modeled and simulated subsystems with physical hardware. In the current work, the electrical power system is implemented in hardware, while the turbomachinery is emulated with EMs driven by a real-time model and controller. Two noteworthy testbeds exist at the National Aeronautics and Space Administration (NASA) where similar work has been conducted [6–8]. The NASA Electric Aircraft Testbed (NEAT) aims to test both sub- and full-scale electrical system components at altitude [9] and the Hybrid Propulsion Emulation Rig (HyPER) aims to test advanced control systems in a sub-scale reconfigurable environment without turbomachinery or rotors/propellers present [10]. The research presented in this paper was conducted in the latter testbed.

Creating an environment for the testing of electrified aircraft propulsion (EAP) controllers without the inclusion of turbomachinery/rotors involves replacing those systems with EMs. A closed-loop control and scaling algorithm, named the Sliding Mode Impedance Controller with Scaling (SMICS) is used in conjunction with a full-scale model to emulate scaled turbomachinery shaft dynamics. An example of this concept is shown in Fig. 2. Prior work by the authors has shown that it is possible to reproduce the sub-scale dynamic behavior of turbomachinery/rotors using EMs [11]. It was also shown that the model used to drive the closed-loop electro-mechanical system under emulation control behaves as it would in a simulation of the full-scale hybrid powertrain [8]. However, the approach used in these applications has limitations that affect the closed-loop dynamical characteristics and thus emulation performance.

The focus of this paper is to alleviate or eliminate the limitations of the SMICS approach by modifying the algorithm and integrating adaptive control into its framework. The updated controller, named the Adaptive Sliding Mode Impedance Controller with Scaling (ASMICS), is tested on the HyPER with the task of emulating the dynamic sub-scale torque loads of the low- and high-pressure turbomachinery shafts of a parallel hybrid-electric version of the Advanced Geared TurboFan 30,000 (AGTF30) [12]. Regulating the operation of the AGTF30 model and the electro-mechanical system is the Turbine Electrified Energy Management (TEEM) control algorithm [13]. This algorithm is tasked with improving turbomachinery operability during transients by utilizing EMs coupled to the low- and high-pressure shafts to modify the turbomachinery operation [14].

The remainder of the paper is organized as follows. Section III outlines the SMICS approach and explains its drawbacks. The benefits of modifying the existing algorithm and integrating adaptive control techniques are also highlighted. Section IV mathematically derives the integration of adaptive control into the SMICS algorithm to form the ASMICS and proves asymptotic stability. Section V details the hardware-in-the-loop test environment and setup as

well as the actuation strategy. Section VI presents the test results using both the SMICS and ASMICS. The turbofan model and emulation controller operation, in both cases, are compared. Additional results are compared showing the performance of the emulation controllers under high and low plant parameter uncertainty conditions. Finally, section VII concludes the paper.

## III. Sliding Mode Impedance Controller with Scaling (SMICS)

This section presents the SMICS design and discusses its limitations. Consider the following scalar, mechanical, dynamic system of a rotating shaft with two EMs mechanically coupled to either side shown in Eq. 1.

$$\dot{\omega}_P = J_P^{-1}[T_M + T_{G_s} - B_P \omega_P] \tag{1}$$

In this system, $\omega_P$ is the angular speed, $\dot{\omega}_P$ is the angular acceleration, $J_P > 0$ is the angular inertia, $T_M$ is the emulation EM torque, $T_{G_s}$ is the research EM torque, and $B_P \geq 0$ is the angular viscous damping coefficient. Sub-scale equivalent variables, denoted with subscript $s$, are defined as:

$$T_{E_s} = \beta T_E \tag{2}$$

$$T_{G_s} = \beta T_G \tag{3}$$

$$J_{E_s} = \alpha^{-1} \beta J_E \tag{4}$$

$$\dot{\omega}_{E_s} = \alpha \dot{\omega}_E = \dot{\omega}_P \tag{5}$$

$$\omega_{E_s} = \alpha \omega_E = \omega_p \tag{6}$$

where $\alpha > 0$ and $\beta > 0$ are the speed and torque scalar coefficients, $T_E$ is the model net turbomachinery torque, $T_G$ is the model EM torque, $\omega_E$ is the model turbofan shaft angular speed, $\dot{\omega}_E$ is the model turbofan shaft angular acceleration, and $J_E$ is the model turbofan shaft angular inertia. The SMICS control law proposed in [11] is:

$$T_M = J_P J_{E_s}^{-1} \left[ T_{E_s} + T_{G_s} + \eta \text{sat}(s, \phi) + K_P s + K_I \int [s] dt + K_D \dot{s} \right] + B_P \omega_P - T_{G_s} \tag{7}$$

where $\eta > 0$ is a scalar gain, and the terms $K_P \geq 0$, $K_I \geq 0$, and $K_D \geq 0$ are proportional, integral, and derivative scalar gains. The sliding surface, $s$, is defined as:

$$s = \int \left[ T_{E_s} + T_{G_s} \right] dt - J_{E_s} \omega_P \tag{8}$$

and the saturation function, sat(), is:

$$\text{sat}(s, \phi) = \begin{cases} \frac{s}{\phi} & |s| \leq \phi \\ \text{sign}(s) & |s| > \phi \end{cases} \tag{9}$$

where $\phi > 0$ is the boundary layer thickness. In accordance with sliding mode control theory, Eq. 7 can be broken down into its reaching law, $\dot{s}$, and equivalent control, $u_{eq}$, components, denoted as:

$$\dot{s} = J_P J_{E_s}^{-1} \left[ \eta \text{sat}(s, \phi) + K_P s + K_I \int [s] dt + K_D \dot{s} \right] \tag{10}$$

$$u_{eq} = J_P J_{E_s}^{-1} \left[ T_{E_s} + T_{G_s} \right] + B_P \omega_P - T_{G_s} \tag{11}$$

Equation 10 was designed to contain integral and derivative components. These components contribute to the first limitation of SMICS, which is no guarantee of asymptotic stability. Subsequent Lyapunov stability analysis of Eq. 7 produces the following Lyapunov derivative:

$$\dot{V}(s) = s \left[ -\eta \text{sat}(s, \phi) - K_P s - K_I \int [s] dt - K_D \dot{s} \right] \tag{12}$$

By inspection, Eq. 12 is shown not to satisfy Lyapunov asymptotic stability criteria [15] due to the presence of the integral and derivative terms. Indeed, one can see that when $s \geq 0$, the derivative and integral terms can be positive,

thus not satisfying the necessary negative-definite or negative semi-definite property of $\dot{V}(s)$. The second limitation of SMICS is its susceptibility to parametric uncertainty, resulting from discrepancies between the assumed and nominal system parameters. Equation 7 requires estimates of $J_P$ and $B_P$, which can be inaccurate and change with time or system operating point. A result of poor system knowledge is an increase in control effort from the reaching law portion of the control design, which is known to cause significant chatter in sliding mode control. Chatter is undesirable high-frequency fluctuations in the control input signal. Indeed, to combat system uncertainty in SMICS, the gains $\eta$, $K_P$, $K_I$, and $K_D$ would require tuning that could lead to chatter. The following section proposes a controller to overcome both limitations i.e. to reduce the contribution of the reaching law in the control input signal and to guarantee asymptotic stability.

## IV. Adaptive Sliding Mode Impedance Controller with Scaling (ASMICS)

In this study, we introduce adaptivity to SMICS to overcome parametric uncertainty and to ensure controller stability. Removing the $K_I$ and $K_D$ terms from the reaching law and re-deriving the control law results in:

$$T_M = J_P J_{E_s}^{-1} \left( T_{E_s} + T_{G_s} - B_{E_s} \omega_P \right) - T_{G_s} + B_P \omega_P - \eta \mathrm{sat}(s, \phi) - K_P s \tag{13}$$

Equation 13 includes the full-scale turbofan shaft angular viscous damping coefficient, $B_E$, where $B_{E_s}$ is defined as:

$$B_{E_s} = \alpha^{-1} \beta B_E \tag{14}$$

$B_E$ is included in the adaptive controller in a case where the effect of viscous damping on a turbomachinery or rotor shaft needs to be emulated. Selecting $J_P$ and $B_P$ as adaptive parameters and substituting their estimates, $\hat{J}_P$ and $\hat{B}_P$, into Eq. 13, produces:

$$T_M = \hat{J}_P J_{E_s}^{-1} \left( T_{E_s} + T_{G_s} - B_{E_s} \omega_P \right) - T_{G_s} + \hat{B}_P \omega_P - \eta \mathrm{sat}(s, \phi) - K_P s \tag{15}$$

Equation 15 is referred to as the Adaptive SMICS (ASMICS), where the reaching law and equivalent control are now defined as:

$$\dot{s} = -\eta \mathrm{sat}(s, \phi) - K_P s \tag{16}$$

$$u_{eq} = \hat{J}_P J_{E_s}^{-1} \left( T_{E_s} + T_{G_s} - B_{E_s} \omega_P \right) - T_{G_s} + \hat{B}_P \omega_P \tag{17}$$

To show that Eq. 15 guarantees closed-loop stability, the following Lyapunov function, V, is proposed:

$$V = V_S + V_{J_P} + V_{B_P} \tag{18}$$

Equation 18 is composed of three components: the sliding mode control portion, $V_S$, and adaptive parameter portions, $V_{J_P}$ and $V_{B_P}$, defined as:

$$V_S = \frac{1}{2} J_E^{-1} J_P s^2 \tag{19}$$

$$V_{J_P} = \frac{1}{2} \gamma_{J_P}^{-1} \tilde{J}_P^2 \tag{20}$$

$$V_{B_P} = \frac{1}{2} \gamma_{B_P}^{-1} \tilde{B}_P^2 \tag{21}$$

where $\gamma_{J_P} \geq 0$ and $\gamma_{B_P} \geq 0$ denote the learning rate gains of $J_P$ and $B_P$. The error terms $\tilde{J}_P$ and $\tilde{B}_P$ describe the difference between the estimated and true value of the adaptive parameters, represented by:

$$\tilde{J}_P = J_P - \hat{J}_P \tag{22}$$

$$\tilde{B}_P = B_P - \hat{B}_P \tag{23}$$

To obtain the Lyapunov function derivative, $\dot{V}$, differentiate Eqs. 19-21:

$$\dot{V}_S = J_E^{-1} J_P s \dot{s} \tag{24}$$

$$\dot{V}_{J_P} = \gamma_{J_P}^{-1} \tilde{J}_P \dot{\hat{J}}_P \tag{25}$$

$$\dot{V}_{B_P} = \gamma_{B_P}^{-1} \tilde{B}_P \dot{\hat{B}}_P \tag{26}$$

Substituting the derivative of Eq. 8 into Eq. 24, multiplying by $\frac{J_P \alpha}{J_E \beta}$, substituting Eq. 15, and simplifying yields:

$$\dot{V}_S = s \left[ J_{E_s}^{-1} \tilde{J}_P \left( T_{E_s} + T_{G_s} - B_{E_s} \omega_P \right) + \tilde{B}_P \omega_P - \eta \mathrm{sat}(s, \phi) - K_P s \right] \tag{27}$$

Selecting the following adaptation laws:

$$\dot{\hat{J}}_P = -\gamma_{J_P} s J_{E_s}^{-1} \left( T_{E_s} + T_{G_s} - B_{E_s} \omega_P \right) \tag{28}$$

$$\dot{\hat{B}}_P = -\gamma_{B_P} s \omega_P \tag{29}$$

substituting Eqs. 27-29 into the derivative of Eq. 18, and simplifying produces:

$$\dot{V} = -s \left[ \eta \mathrm{sat}(s, \phi) + K_P s \right] \tag{30}$$

Since $\dot{V} < 0$ when $s \neq 0$ and $\dot{V} = 0$ when $s = 0$, the closed-loop system is asymptotically stable in the sense of Lyapunov.

## V. Implementation

The SMICS and ASMICS algorithms were implemented on the NASA Hybrid Propulsion Emulation Rig (HyPER), which is a sub-scale electro-mechanical system built to verify EAP control concepts and algorithms on sub-scale hardware representations of EAP powertrains [10]. Figure 3 provides several views of HyPER. This 100 kW electro-mechanical system incorporates four EMs, four inverter/motor controllers, one direct current to direct current (DC-DC) converter, and a supercapacitor bank consisting of three supercapacitors in series. The EMs in this system are permanent magnet synchronous machines (PMSMs). These PMSMs are configured into two pairs with the units in each pair connected mechanically by a shaft. pairs of PMSMs are mechanically connected by a shaft. All PMSMs are electrically coupled to an inverter/motor controller. One PMSM from each pair emulates the engine shaft dynamic load, while the other is part of the experimental scaled electric powertrain. Two electrical buses are present: one representing the scaled electrical powertrain bus, and the other supplying/sourcing power to/from the emulation PMSMs. A bi-directional power supply is present on each bus. The power supply connected to the former bus is not used in this testing. The experimental bus includes a super-capacitor bank coupled to a DC-DC converter. The electro-mechanical system architecture is included in the HyPER representation shown in Fig. 4.

A unique feature of HyPER is the absence of large rotating aircraft propulsion components such as turbo-machinery or rotors/propellers. Torque loads of these components are emulated using EMs that receive commands from either the SMICS or ASMICS. The SMICS and ASMICS algorithms enable HyPER to have sub-scale mechanical dynamical characteristics of the component of choice. When commanded using a full-scale component model and its controller, HyPER behaves with sub-scale shaft speed dynamic responses that are linearly scalable to the component model scale. In other words, the SMICS and ASMICS algorithms provide the interface between the sub-scale electro-mechanical system hardware and the full-scale propulsion system models and reconcile the dynamic differences between the two. This concept is illustrated graphically in the control implementation diagram in Fig. 5. From the point of view of the EAP control system under test, it is actuating a full-scale EAP system with full-scale dynamical characteristics. In reality, it is actuating a sub-scale electro-mechanical system representation of the propulsion system without turbomachinery. In this study, HyPER is configured to represent the hybrid-electric propulsion system of the AGTF30 with the TEEM concept and control approach. The configuration is represented in Fig. 4. The two EMs and



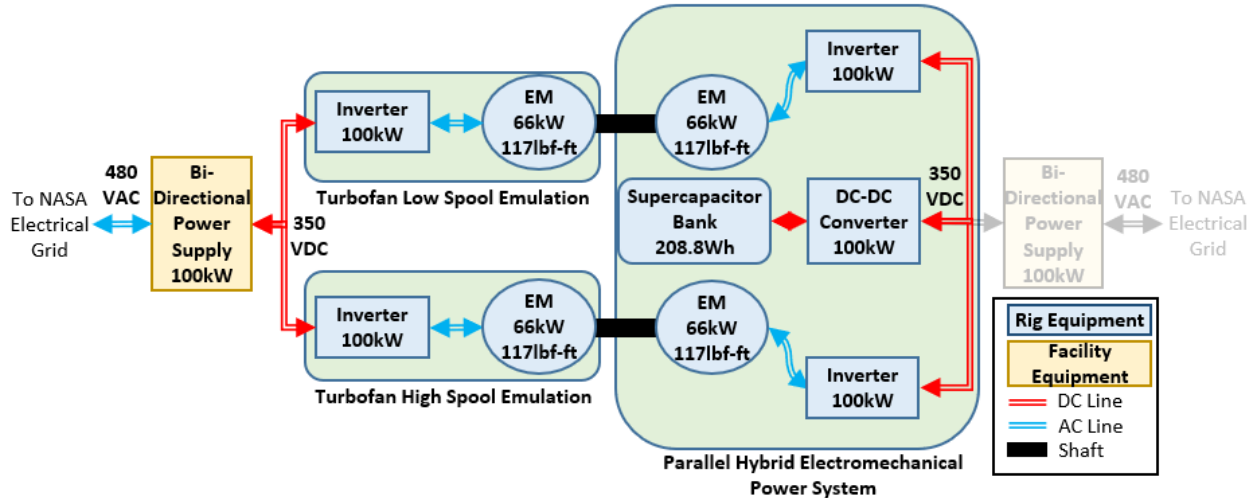**Fig. 3    Hybrid Propulsion Emulation Rig (HyPER)**

**Fig. 4 HyPER configured to represent the parallel hybrid-electric AGTF30 turbofan engine.**

inverter/motor controllers contained in the green boxes
on the left side of the diagram emulate the sub-scale low spool (LS) and high spool (HS) turbomachinery torques of
the AGTF30. The electro-mechanical system contained in the green box on the right represents the sub-scale parallel
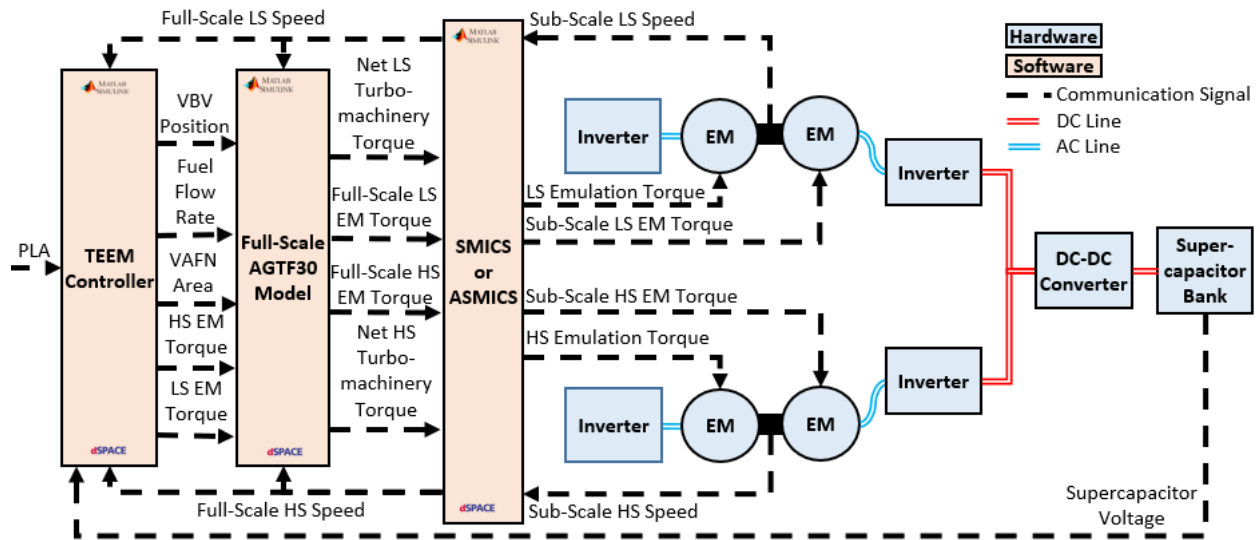hybrid-electric electro-mechanical system architecture of the AGTF30.



**Fig. 5 Control diagram of AGTF30 implementation in HyPER.**

Three separate tests were conducted using different control structures. The tests are the following:
  (a) A software-in-the-loop (SIL) test, where the parallel hybrid electrical system model and TEEM control actuates
       full-scale models of the AGTF30 low- and high-pressure shafts.
  (b) A hardware in the loop (HIL) test where the full-scale AGTF30 model with TEEM control actuates HyPER
       hardware in closed loop with the SMICS.
  (c) A hardware in the loop (HIL) test identical to (b) except with the SMICS replaced by the ASMICS.
The descriptions of the tests in the above list are illustrated in Fig. 6. The SMICS and ASMICS controllers were
tested by commanding an idle to full throttle and followed by a full throttle to idle power lever angle (PLA) change
to the AGTF30 model at sea-level-static conditions (altitude of 0 ft, Mach number of 0, and no change in the defined
ambient temperature at the altitude and Mach number conditions), shown in Fig. 7. Both the SMICS and ASMICS, the
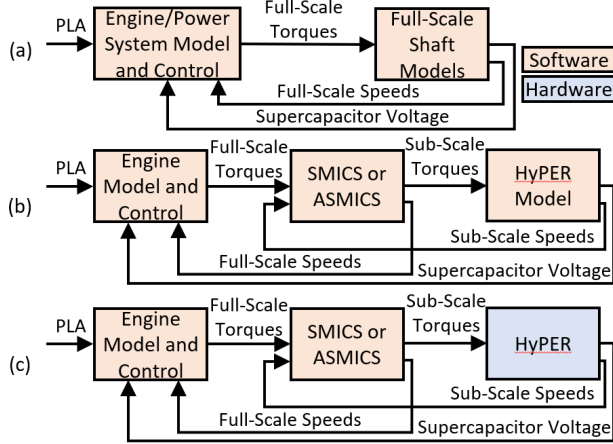
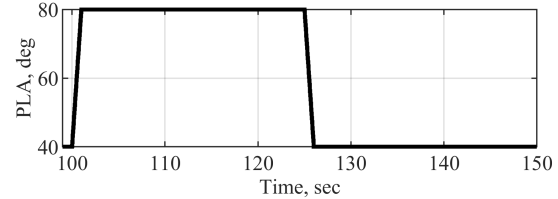**Fig. 6   Control diagrams representing the three types of tests to be compared.**



**Fig. 7   Power lever angle (PLA) command to AGTF30 model.**

AGTF30 turbofan model, and the TEEM controller are implemented in the MATLAB®/Simulink® environment. The implementation was ran in real-time using a dSPACE® SCALEXIO® real-time computer system with a time step of 15 milliseconds. To mitigate parameter drift, the ASMICS controller features a deadzone, a commonly implemented solution for this phenomenon in adaptive control [16].

# VI. Results

A performance comparison between the SMICS and ASMICS is conducted from the point of view of the AGTF30 engine model, and tests (b) and (c) are compared to (a). The root-mean-squared relative error (RMSRE), defined in Eq. (31), is used to evaluate performance between SIL and HIL results. The RMSRE metric compares the relative error between the HIL and SIL results for the chosen variable, $x$. The HIL and SIL results are denoted with subscripts $HIL$ and $SIL$, respectively. The sample number and total number of samples are denoted as $i$ and $N$, respectively.

$$\text{RMSRE} = 100\sqrt{\frac{1}{N}\sum_{i=1}^{N}\left(\frac{x_{HIL} - x_{SIL}}{\max(|x_{SIL}|)}\right)^2} \tag{31}$$

The conventional relative error equation contains only $x_{SIL}$ in the denominator. The $\max(|x_{SIL}|)$ term is used instead to ensure the denominator magnitude is non-zero. The metric for comparing the difference between the RMSRE percentages for the SMICS vs. SIL and ASMICS vs. SIL comparison results is the relative error (RE). The RE used for this purpose is defined in Eq. (32). The subscripts $SMICS$ and $ASMICS$ denote variables relating to the results using the SMICS and ASMICS controllers, respectively.

$$\text{RE} = 100\left(\frac{\text{RMSRE}_{\text{ASMICS}} - \text{RMSRE}_{\text{SMICS}}}{\text{RMSRE}_{\text{SMICS}}}\right) \tag{32}$$

Table 1 displays the resultant RMSREs and REs for selected key AGTF30 actuator, sensor, engine performance, and solver performance variables.

Insignificant increases and decreases in the RE of the various parameters relative to the magnitude of the RMSRE percentages are observed. Variables with large RMSRE percentages and large RE percentages are considered significant. Significant variables are the HS EM torque and the iteration count, which had a 51.2% and 31.5% reduction, respectively. Figure 8 shows the HS EM torque and iteration count variables. Note that the plots in Fig. 8 and subsequent figures display the responses from 100-150 seconds. Prior to 100 seconds is a startup period where the electric machines are driven to initial speeds and torques that are compatible with the initial state of the turbofan model. Control is then handed to the turbofan model. Although the SMICS or ASMICS is enabled during this period, it is not considered in the analyses. From Fig. 8, it is evident that significantly large RE in the HS EM torque is due to the difference in the torque application during the acceleration. This is shown in the magnified inset of the HS EM Torque in Fig. 8,

8

**Table 1    Changes in key AGTF30 Model variables**

| Variable | RMSRE, % SIL vs. HIL | | RE, % |
|---|---|---|---|
| | SMICS | ASMICS | |
| Fuel Flow Rate | 0.055% | 0.044% | -20.0% |
| VBV Position | 0.333% | 0.372% | +11.7% |
| VAFN Area | 0.055% | 0.048% | -12.7% |
| LS EM Torque | 0.871% | 0.813% | -6.6% |
| HS EM Torque | 2.001% | 0.975% | -51.2% |
| LS Speed | 0.139% | 0.142% | +2.1% |
| HS Speed | 0.098% | 0.116% | +18.3% |
| LPC Stall Margin | 1.175% | 1.464% | +24.5% |
| HPC Stall Margin | 0.397% | 0.422% | +6.2% |
| LPC Output Static Pressure | 0.104% | 0.074% | -28.8% |
| HPT Inlet Total Temperature | 0.048% | 0.023% | -52.1% |
| Thrust | 0.180% | 0.202% | +12.2% |
| Iteration Count | 40.025% | 27.413% | -31.5% |
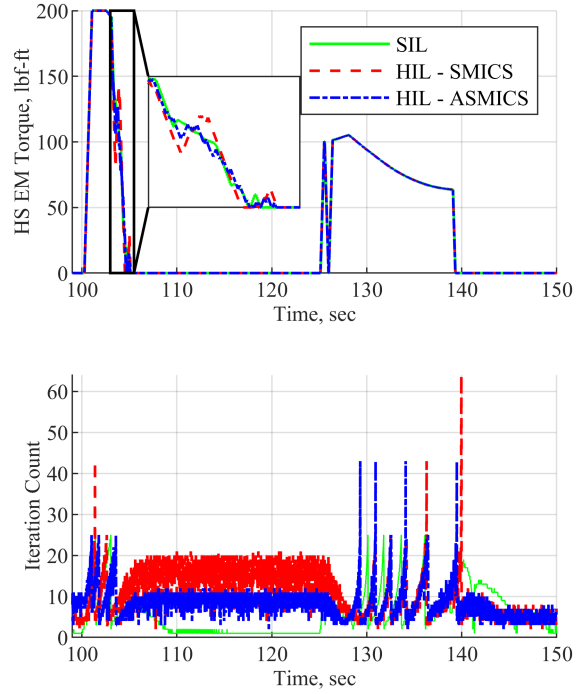


**Fig. 8    HS EM torque and iteration count.**

where the SMICS torque oscillates around the SIL torque as compared to the ASMICS torque which more closely aligns with the SIL data. This phenomenon is likely caused by the inability of SMICS to achieve the nominal dynamic characteristics due to its reliance on parameter certainty. This results in the AGTF30 TEEM controller actuating the HS EM in an undesirable manner, impacting the HS EM torque. It is noteworthy to state that both the average and peak iteration counts throughout the test decreased significantly. Lessening the number of average iterations and peak iteration counts reduces the likelihood of non-convergences in the numerical solution of the AGTF30 engine model and mitigates violation of real-time calculation constraints.

Figure 9 displays the resultant controller trajectories for the high and low spools, where the sliding surface, $s$, reaching law, $\dot{s}$, equivalent control, $u_{eq}$, the angular inertia estimate, $\hat{J}_P$, and the angular viscous damping coefficient estimate, $\hat{B}_P$, are plotted. The parameters $\hat{J}_P$ and $\hat{B}_P$ were initialized at 0.0594 lbf-ft-s$^2$ and 0.04 lbf-ft-s, respectively, for both the high and low spools. Both controllers maintain similar magnitudes around the sliding surface, with brief excursions occurring with SMICS between 100-110s on the high spool. However, the $\dot{s}$ and $u_{eq}$ components highlight the difference in the controllers. Because SMICS operates with assumed constant estimated values for $\hat{J}_P$ and $\hat{B}_P$, which may differ from the true system values, high levels of torque are commanded in the equivalent control portion of the control signal. This demand causes the reaching law component, $\dot{s}$, to also command a large control effort of nearly opposite magnitude to counteract the parametric discrepancy. As previously mentioned, high control demand in the reaching law can lead to increased chatter in the control signal and should be avoided. Comparatively, ASMICS maintains low control effort in the reaching law and equivalent control components. Because the controller can adapt $J_P$ and $B_P$, it uses a more accurate system model, leading to the equivalent control demanding less torque. In response, the reaching law does not counteract $u_{eq}$ but rather maintains a near zero torque for the duration of the experiment. This response holds across both spools, where the parameter adaptation profiles appear to be similar for $\hat{J}_P$ and slightly different for $\hat{B}_P$. Indeed, the viscous damping coefficient seems sensitive to changes in $u_{eq}$, as seen on the high spool where $B_P$ increases suddenly shortly after 100s as the equivalent control decreases suddenly in the same timeframe. Further investigation into the sensitivity of the parameters to control action is warranted.

To investigate the impact of parametric uncertainty on the controllers, HIL tests were conducted at both low and high parameter uncertainty conditions with both SMICS and ASMICS. At low uncertainty (LU), the parameters $J_P$
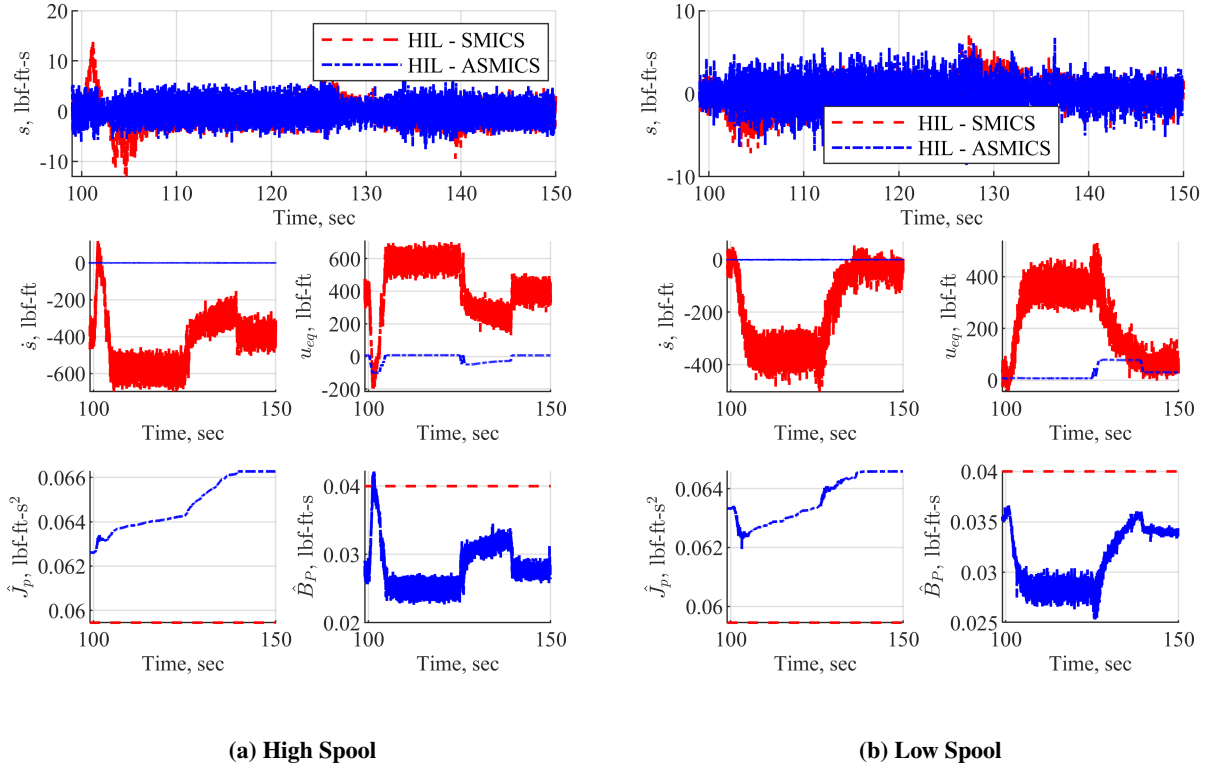
9

**(a) High Spool**

**(b) Low Spool**

**Fig. 9** **Sliding surface ($s$), reaching law ($\dot{s}$), equivalent control ($u_{eq}$), estimated angular inertia ($\hat{J}_P$), and estimated angular viscous damping coefficient ($\hat{B}_P$) responses with SMICS and ASMICS applied on the high spool (left) and low spool (right).**

and $B_P$ were selected to be as close to the known plant parameters as possible, initialized at the previously defined initial conditions for $\hat{J}_P$ and $\hat{B}_P$. At high uncertainty (HU), the parameters $J_P$ and $B_P$ were selected to be twice their low uncertainty value, resulting in the values 0.1189 lbf-ft-s$^2$ and 0.08 lbf-ft-s, respectively. The results are plotted for the low and high spool emulation controllers in Figs. 10a and 10b, where the emulation EM torque, the sliding surface, the reaching law, and the equivalent control are displayed. Note that all signals have noticeable levels of noise present in their response. As previously seen, SMICS is susceptible to parameter discrepancy, leading to high magnitude equivalent control and reaching law components that sum to the total $T_M$ signal. The results in Fig. 10a show high susceptibility to increased uncertainty, as the magnitude of the control law components increases with greater uncertainty, where the demand at high uncertainty is seen to be approximately three times larger than the low uncertainty case. As previously mentioned, high control demand in the reaching law can lead to increased chatter in the control signal. While the noise in the data makes it challenging to identify chatter, the $T_M$ response seems to highlight this outcome. The magnified inset shows how as the uncertainty grows from low to high, the fluctuations in the control signal broaden. Assuming the noise is constant across each HIL test, then this outcome is most likely due to increased chatter in SMICS due to increased $\dot{s}$ contribution. ASMICS does not exhibit the same susceptibility to parametric uncertainty as SMICS. As the uncertainty increases from low to high, ASMICS exhibits the same magnitude $\dot{s}$ and $u_{eq}$ response. As shown in the $T_M$ response in Fig. 10b, although the ASMICS control response spreads across a larger magnitude than the SMICS response, it does not increase as the uncertainty increases. This response is very beneficial and implies that in the presence of incomplete system knowledge, the controller can avoid exciting high frequency dynamics to maintain system performance at the price of minimally higher overall control effort. By adapting for the $J_P$ and $B_P$ terms, ASMICS can avoid inducing chatter, thus avoiding a pitfall of SMICS.
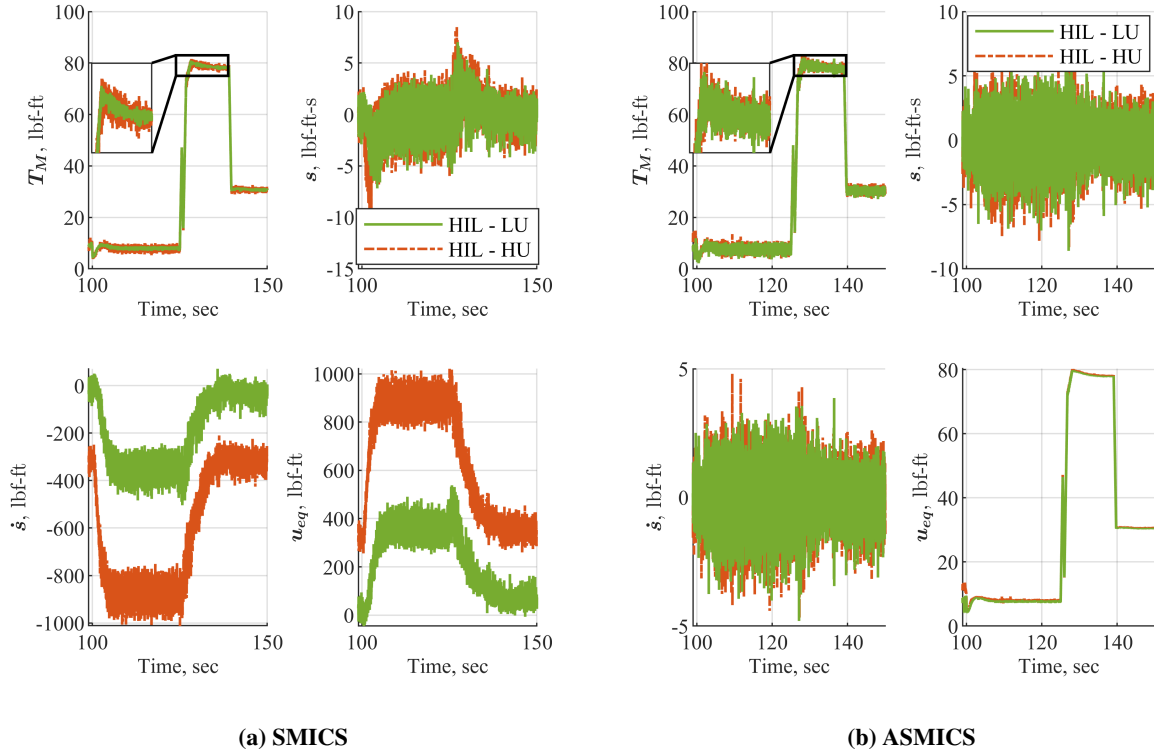
**(a) SMICS**

**(b) ASMICS**

**Fig. 10 Emulation machine torque ($T_M$), sliding surface ($s$), reaching law ($\dot{s}$), and equivalent control ($u_{eq}$) responses with SMICS (left) and ASMICS (right) applied to the low spool.**

## VII. Conclusion

An extension to a control and scaling approach used to enable the verification of EAP control algorithms using a sub-scale electro-mechanical system without turbomachinery is presented. SMICS, the original approach, replaces the low and high spools of a turbofan with a full-scale model of a turbofan, an emulation controller, and EMs to represent its dynamical loading on a sub-scale parallel hybrid electro-mechanical system. ASMICS, the extension, integrates adaptive control to guarantee asymptotic stability and reduce the effects of parameter uncertainty on the emulation controller performance. The original and extended controller were tested using a novel hybrid-electric propulsion system controller, a turbofan model, and a sub-scale electro-mechanical system representing a parallel hybrid-electric turbofan architecture. Performance comparisons found the extended controller able to increase the accuracy of key performance variables within the turbofan model compared to a theoretical baseline. This result highlights that adding adaptivity to the original design is beneficial, permitting the extended controller to actuate with a more accurate system model under test conditions. Subsequent robustness analysis demonstrated that in the face of up to 100% parameter degradation in the assumed plant parameters, the extended controller functioned with minimal performance change unlike its original counterpart.

# References

[1] "Strategic Plan Fiscal Year 2022-2026," *U.S. Department of Transportation*, Washington, D.C., 2022. URL `https://www.transportation.gov/sites/dot.gov/files/2022-04/US_DOT_FY2022-26_Strategic_Plan.pdf`.

[2] "Research, Development, and Technology Strategic Plan Fiscal Year 2022-2026," *U.S. Department of Transportation*, Washington, D.C., 2022. URL `https://www.transportation.gov/sites/dot.gov/files/2023-01/USDOT%20RDT%20Strategic%20Plan%20FY22-26_010523_508.pdf`.

[3] "NASA 2022 Strategic Plan," *National Aeronautics and Space Administration*, Washington, D.C., 2022. URL `https://www.nasa.gov/wp-content/uploads/2023/09/fy-22-strategic-plan-1.pdf`.

[4] "Flight Plan 21 Fiscal Year 2022-2026," *Federal Aviation Administration*, Washington, D.C., 2022. URL `https://www.faa.gov/sites/faa.gov/files/Flight%20Plan%2021_2022_0.pdf`.

[5] Kenyon, J. A., "NASA Sustainable Flight National Partnership," *AIAA Science and Technology (SciTech) Forum*, San Diego, CA, 2022. URL `https://ntrs.nasa.gov/api/citations/20210026294/downloads/2022%2001%2006%20Kenyon%20SCITECH%20Spotlight%20on%20Aviation%20Panel.pdf`.

[6] Sachs-Wetstone, J. J., Bianco, S. J., Kratz, J. L., Horning, M. A., Amthor, A. E., Connolly, J. W., and Saus, J. R., "Hybrid-Electric Aero-Propulsion Controls Testbed Results," *AIAA Aviation/Electric Aircraft Technologies Symposium (EATS) Forum*, San Diego, CA, 2023. https://doi.org/https://doi.org/10.2514/6.2023-4233.

[7] Simon, D. L., Bianco, S. J., Horning, M. A., Saus, J. R., Amthor, A. E., and Sachs-Wetstone, J. J., "Real-time Hardware-in-the-Loop Evaluation of a Partially Turboelectric Propulsion Control Design," *AIAA Aviation/Electric Aircraft Technologies Symposium (EATS) Forum*, San Diego, CA, 2023. https://doi.org/https://doi.org/10.2514/6.2023-4235.

[8] Bianco, S. J., Kratz, J. L., Culley, D. E., Buescher, H. E., Horning, M. A., Saus, J. R., Sachs-Wetstone, J. J., and Connolly, J. W., "Hybrid-Electric Aero-Propulsion Controls Testbed Results with Energy Storage," *AIAA Aviation Forum/Electric Aircraft Technologies Symposium (EATS)*, San Diego, CA, 2023. https://doi.org/https://doi.org/10.2514/6.2023-4234.

[9] Haglage, J. M., and Brown, T. E., "NASA Electric Aircraft Testbed (NEAT) Reconfiguration to Enable Altitude Testing of Megawatt-Scale Electric Machines," *AIAA/IEEE Electric Aircraft Technologies Symposium (EATS)*, New Orleans, LA, 2020. URL https://ieeexplore.ieee.org/document/9235179.

[10] Buescher, H. E., Culley, D. E., Bianco, S. J., Connolly, J. W., Dimston, A. E., Saus, J. R., Theman, C. J., Hunker, K. R., Garrett, M. J., Haglage, J. M., Horning, M. A., Cha, Y. C., and Purpera, N. C., "Hybrid-Electric Aero-Propulsion Controls Laboratory: Overview and Capability," *AIAA Science and Technology (SciTech) Forum*, National Harbor, MD, 2022. https://doi.org/https://doi.org/10.2514/6.2023-0671.

[11] Bianco, S. J., and Simon, D. L., "Control and Scaling Approach for the Emulation of Dynamic Subscale Torque Loads," *AIAA Aviation Forum/Electric Aircraft Technologies Symposium (EATS)*, San Diego, CA, 2023. https://doi.org/https://doi.org/10.2514/6.2023-4232.

[12] Chapman, J. W., and Litt, J. S., "Control Design for an Advanced Geared Turbofan Engine," *AIAA Propulsion and Energy Forum*, Atlanta, GA, 2017. https://doi.org/https://doi.org/10.2514/6.2017-4820.

[13] Kratz, J. L., Culley, D. E., and Thomas, G. L., "A Control Strategy for Turbine Electrified Energy Management," *AIAA Propulsion and Energy Forum*, Indianapolis, IN, 2019. https://doi.org/https://doi.org/10.2514/6.2019-4499.

[14] Culley, D. E., Kratz, J. L., and Thomas, G. L., "Turbine Electrified Energy Management (TEEM) For Enabling More Efficient Engine Designs," *AIAA Propulsion and Energy Forum*, Cincinnati, OH, 2018. https://doi.org/https://doi.org/10.2514/6.2018-4798.

[15] Lyapunov, A. M., "The General Problem of the Stability of Motion," *International Journal of Control*, Vol. 55, No. 3, 1992, pp. 531–534. https://doi.org/https://doi.org/10.1080/00207179208934253.

[16] Slotine, J.-J. E., and Li, W., *Applied Nonlinear Control*, Prentice-Hall, Englewood Cliffs, N.J., USA, 1991.